Catalysis Science & Technology

ROYAL SOCIETY OF CHEMISTRY

PAPER

View Article Online
View Journal | View Issue



Cite this: *Catal. Sci. Technol.*, 2024, **14**, 5624

# Ligand coordination controlled by monomer binding: a hint from DFT for stereoselective lactide polymerization†

Massimo Christian D'Alterio, [a] Serena Moccia, [a] Yolanda Rusconi, [b] Claudio De Rosa [a] and Giovanni Talarico *[ab]

Stereoselective ring opening polymerization (ROP) of racemic lactide (*rac*-LA) is a challenging goal because a rationale connecting the catalyst structure and polymer microstructure (as has been established for α-olefin polymerization) is still missing. In this work, we reveal the origin of the stereoselective preference for D and L-lactide with two enantiopure salen–Al complexes, which have so far been claimed as the most efficient in enantiomorphic site control, using Density Functional Theory calculations. We introduce active site reorganization and monomer/chain switching throughout the reaction pathway, unconventional aspects necessitating careful consideration when confronting the intricacies associated with chiral catalyst recognition. We show how the catalytic pocket easily rearranges in the reaction path establishing a novel concept of the ligand coordination controlled by monomer binding. The resulting final picture of PLA stereoselectivity is much more complex than that of α-olefin polymerization catalysis, and a "complete" prediction by brute-force is (currently) hard, but the principles evolving should – even in their incomplete form – be useful in the design of new selective catalysts.

Received 29th July 2024,
Accepted 5th August 2024

DOI: 10.1039/d4cy00937a

rsc.li/catalysis



## 1. Introduction

The aliphatic polyester poly(lactide) (PLA) has gained increasing popularity as an environmentally friendly substitute for conventional olefin-based plastics, owing to its distinctive attributes of biorenewability, biocompatibility, and biodegradability.[1–4] The PLA life-cycle assessment has shown a consistent reduction in non-renewable-energy compared with petrochemical-derived polymers such as polypropylene and can be recycled and degraded in its end-of-life fate.[1]

The lactide (LA) monomer has two chiral centers and, as a consequence, three diastereoisomers, namely D-LA (*RR*), L-LA (*SS*) and *meso*-LA (*RS*). The homopolymerization of a single enantiomer by ring opening polymerization (ROP) results in an isotactic polymer whereas the stereocontrolled ROP of *rac*- and *meso*-lactide utilizing metal complexes as initiators may lead to a wider range of polymer microstructures (Scheme 1).[5,6] Analogous to α-olefin polymerization transition metal (TM) catalysis,[7–10] the ROP stereochemistry can be dictated by either the enantiomorphic site control (ESC) mechanism, where catalyst chirality dictates homochiral preference, or the chain-end control (CEC) mechanism, where the preference for homochirality or heterochirality depends on the last inserted monomer unit.[11] Indeed, the stereochemistry influence on the physical and mechanical properties of PLA materials has been carefully assessed, and manipulating the microstructure becomes pivotal for tailoring PLA properties with the aim to replace polyolefins in target applications.[12] However, simple relationships between ligand catalysts/PLA microstructures are not yet achieved[13–20] diversely from the α-olefin counterpart where the polymer microstructure can be finely tuned by suitable ligand catalyst modification *a priori*.[21]

In a seminal study of Spassky *et al.*,[22] the enantiomerically pure binaphthyl–salen aluminum complex (system (*R*)-**1**, Scheme 2) was employed for the synthesis of a block copolymer poly(D-lactide)–poly(L-lactide) [(PDLA–PLLA)$_n$] using *rac*-LA monomer feed. Indeed, system (*R*)-**1** revealed, for the first time, a clear ESC preference toward D-LA rather than L-LA ($k_{RR}/k_{SS}$ = 20, Scheme 2), with the formation of a stereocopolymer due to the incorporation of L-LA at a high conversion rate, when the reaction mixture is poor in D-LA. Relevant insights have been later reported by Coates *et al.* by using *rac*-**1** for *rac*-LA polymerization still obtaining isotactic-enriched PLA with a high melting temperature ($T_m$ = 179–191 °C) even at low conversion.[23] The formation of a stereoblock microstructure at low conversion was explained by assuming a polymer chain exchange among the two enantiomeric forms of *rac*-**1** catalysts.[23] Interestingly, Feijen *et al.*[24]

[a] *Department of Chemical Sciences, Università Degli Studi Di Napoli Federico II, Via Cintia, 80126 Napoli, Italy. E-mail: talarico@unina.it*
[b] *Scuola Superiore Meridionale, Largo San Marcellino 10, 80138 Napoli, Italy*

† Electronic supplementary information (ESI) available. See DOI: https://doi.org/10.1039/d4cy00937a

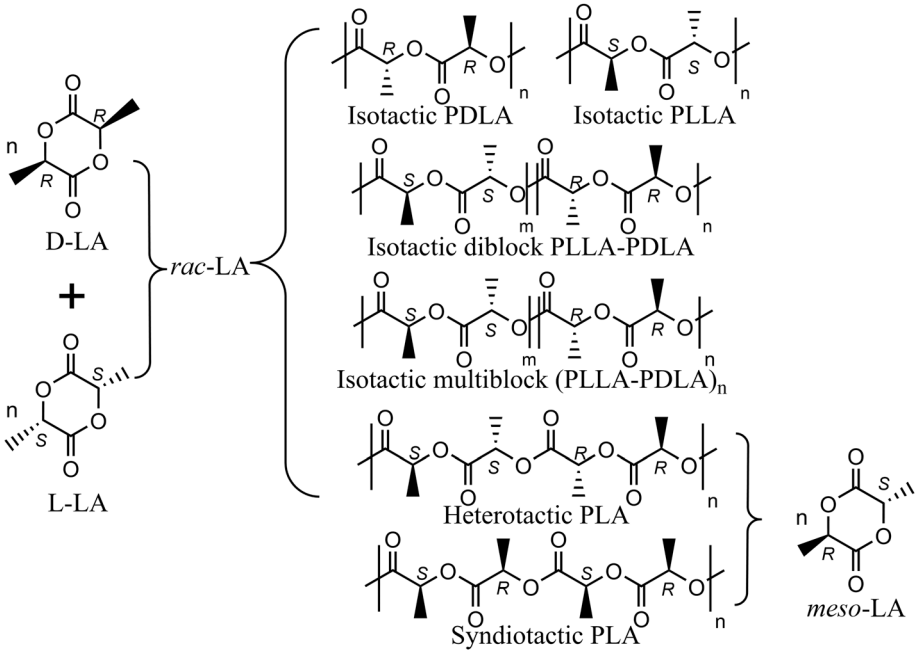


**Scheme 1** Ordered microstructures from stereoselective ROP of *rac*-LA and *meso*-LA.

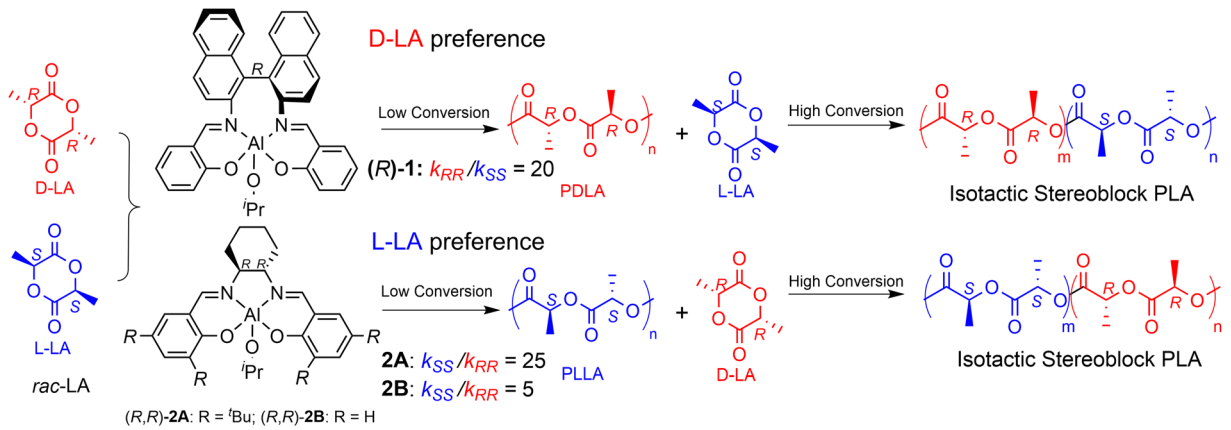


**Scheme 2** Stereoselective ROP behavior of (*R*)-**1** and (*R*,*R*)-**2** toward *rac*-LA.

demonstrated that the enantiopure aluminum complexes incorporating a Jacobsen ligand ((*R*,*R*)-**2A**, Scheme 2) also exhibited significant isoselectivity in *rac*-LA ROP by ESC but with a clear preference toward L-LA ($k_{SS}/k_{RR}$ = 25, Scheme 2). As mentioned for system (*R*)-**1**, the progressive increase in the relative concentration of the D-LA isomer within the monomer pool, ascribed to the initial L-LA transformation into PLLA, results into a stereosequence gradient, transitioning from extended isotactic L-lactyl units to extended isotactic D-lactyl units. Finally, the enantioselectivity dramatically drops when the $^{t}$Bu moieties in the *ortho* position are substituted with H atoms (Scheme 2), as recently reported by Wang and coworkers ($k_{SS}/k_{RR}$ = 5, Scheme 2 for ((*R*,*R*)-**2B**).[25]

Inspired by these results, the enantiomeric resolution and stereoselective polymerization of *rac*-LA have become a challenge in the last two decades with the final target to achieve high levels of isoselectivity combined with an enhanced productivity.[26–30]

However, factors governing ESC and CEC for ROP mechanisms, as well as the interplay between those two stereocontrol mechanisms remain obscure.[31,32] In our recent communication,[33] we anticipated that the origin of the stereoselectivity in *rac*-LA ROP achieved by the enantiopure system (*R*)-**1** is different from the classical ES reported so far. Novel mechanistic steps have been used to trace the experimental stereoselectivity as summarized in Scheme 3. This (remarkable) complexity is due to several factors: 1) multiple ligand wrapping modes at the aluminum center; 2) variations of the wrapping mode configurations during the ROP catalytic cycle; 3) rate limiting step (RLS) energetics dependent on the monomer (D and L) LA as well as on the

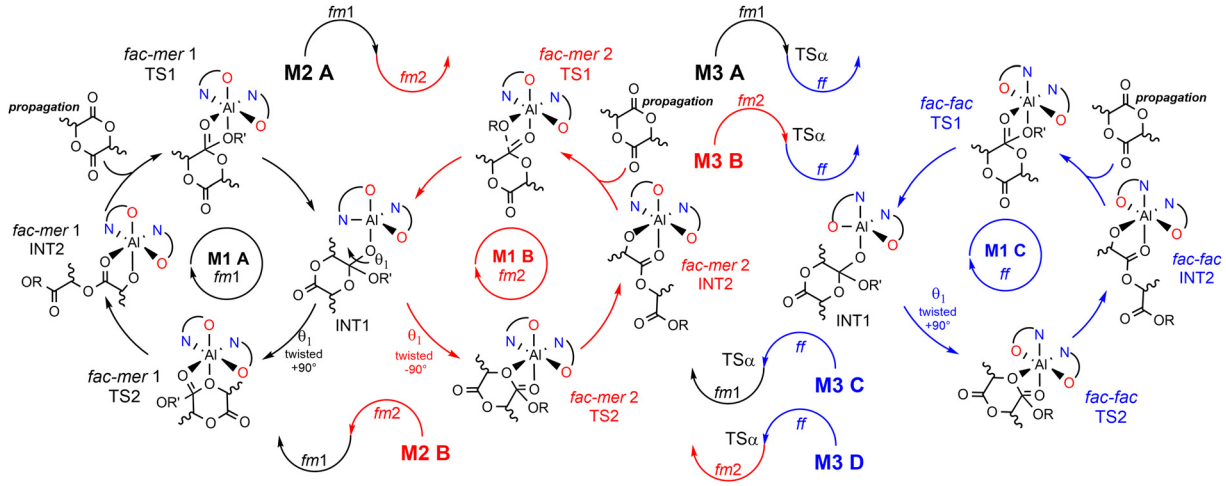


**Scheme 3** Stereoselective ROP of *rac*-LA at an octahedral aluminum center following the mechanistic paths depending on the wrapping mode. **M1-A** (TS1 and TS2 at *fm*1) is reported in black; **M1-B** (TS1 and TS2 at *fm*2) in red and **M1-C** (TS1 and TS2 at *ff*) in blue. Additional mechanisms (**M2-A** and **M2-B**) where TS1 and TS2 show *fm*1 and *fm*2 configurations are reported in half black–half red and half red–half black, respectively, sharing the same INT1.

chirality of the last inserted unit in the growing chain.[34] This complicated scenario makes the prediction of the stereoselective ROP of *rac*-LA a challenging game for chemists[31] and justifies the lack of ligand structure/polymer microstructure relationships as consolidated in stereoselective TM catalyzed olefin polymerization.[7,10,21] Going into more detail, we found that the ligand wrapping mode for (*R*)-**1** may assume *fac–mer* 1 (*fm*1), *fac–mer* 2 (*fm*2) and *fac–fac* (*ff*) configurations and they may interconvert going from the nucleophilic addition (TS1) to the ring opening (TS2) steps.

We identified several reaction paths under the assumption that for the first mechanism (**M1**), both TS1 and TS2 occur with the same wrapping mode (*fm*1, *fm*2 or *ff*, **M1-A**, **M1-B**, **M1-C**, respectively). For the second mechanism (**M2**), TS1 occurs at *fm*1 and TS2 at *fm*2 and *vice versa* (**M2-A** and **M2-B**, respectively). The third mechanism, (**M3**), based on the interconversion among *fac-mer* and *fac-fac*, is also possible but it requires an additional TS that involves active site reorganization *via* the modification of the $O_L$–Al–$O_L$ valence angle (defined as $\alpha$) (see later).

The aim of this work is to furnish, by using computational methods rooted into Density Functional Theory (DFT), a comprehensive analysis of the ESC mechanism(s) for the stereoselective ROP of *rac*-LA promoted by (*R*)-**1** and (*R*,*R*)-**2A** to understand the key factors leading to asymmetric kinetic resolution polymerization (AKRP) processes[35] for D and L-LA. We will elucidate how the two enantiopure salen–Al complexes, despite the ligand/metal similarity, act inversely in the AKRP of *rac*-LA (Scheme 2). The structural features of the ligands, the mechanistic ROP intricacies and the role of the chirality of the growing polymer chain will be analyzed. We will also highlight the microstructure differences derived from our DFT calculations for the so-called stereoblock PLAs promoted by enantiopure (*R*)-**1** and (*R*,*R*)-**2A** complexes. Finally, a novel concept for the stereoselective ROP of *rac*-LA will be defined, aiming to establish ligand catalyst/PLA microstructure relationships.

## 2. Methods

DFT results were obtained using the B3LYP/6-311G(d,p)/SVP level of theory for geometry optimization and the energies were refined by single point calculations with B3LYP-D3BJ(CPCM)/6-311G(d,p). This approach was already tested in the stereoselective ROP[33,36,37] of LA and regioselective methyl glycolide[38] as well as conventional olefin polymerization showing a good match with the experimental results.[39–41] Details are reported in the ESI.†

## 3. Results

### 3.1 Stereoselective *rac*-LA ROP promoted by (*R*)-1

The simplified energetic paths explaining the ROP origin of the stereoselectivity toward *RR*-LA promoted by (*R*)-**1** is reported in Fig. 1. We report the minimum energy pathways (MEPs) of the isotactic enchainment for *RR*- and *SS*-LA insertions with the active species in the preferred ligand coordination modes (*fm* for *RR*-LA and *ff* for *SS*-LA, respectively) extracted from a combinatorial analysis of all the elements of chirality occurring in this reaction, also including the prochirality of the monomer (Scheme S1†). In the context of the classical **M1-A** mechanism in which the catalyst is in *fm*1 wrapping mode, DFT calculations did not reveal any preference for *RR- versus SS*-LA insertion promoted by (*R*)-**1**. In fact, the calculated Gibbs energy values ($\Delta G$) of the RLS for *RR*-LA propagation are very close to those for *SS*-LA (16.4 and 16.2 kcal $mol^{-1}$, Fig. 1). The experimental preference for *RR*-LA is matched only by assuming novel

 

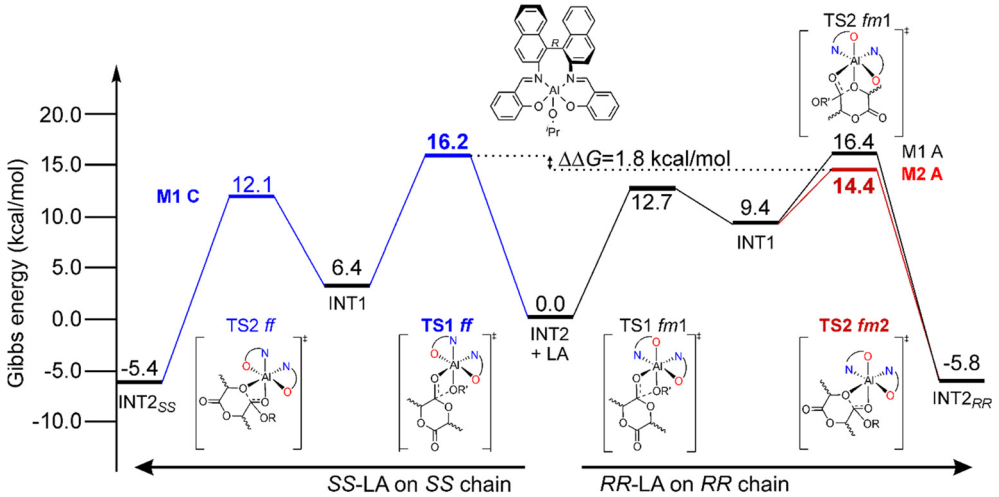


**Fig. 1** Preferred Gibbs energy paths for *RR*-LA (right) and *SS*-LA (left) propagations promoted by (*R*)-**1** following the **M1**–**M2** mechanisms. The RLSs for the reaction paths (see text) are reported in bold.

mechanisms as **M2-A** (TS1 *fm*1 and TS2 *fm*2) and/or **M3-A** (ligand re-organization going from *fm* TS1 to *ff* TS2).

In Scheme 3, we draw the (easy) interconversion between *fm*1 and *fm*2 wrapping modes going from TS1 to TS2. In detail, this interconversion is possible through a barrierless rotation at INT1 around the dihedral angle indicated as $\theta_1$ and involves a single bond (Scheme 3). This mechanism is particularly noteworthy since it enables the catalysts to find the lowest energy paths among the various accessible on the potential energy surface, particularly when the ring opening step (TS2) shows remarkable differences in the Gibbs energies depending on the ligand wrapping mode (Fig. 1). The DFT geometries of these two TSs are reported in Fig. 2 and the main steric interactions leading to the TS2 energetic preference for *fm*2 (Fig. 2A) *vs.* *fm*1 (Fig. 2B) configurations are indicated with arrows.

The steric maps obtained with a molecular descriptor (% $V_{Bur}$)[42–44] reported in Fig. 3 may help to visualize the (*R*)-**1** ligand features leading to the energetic differences reported in Fig. 2. Indeed, the key aspect of the Spassky ligand is the binaphthyl linker (see the red zone in Fig. 3) that is closer to the monomer moiety in TS2 having an *fm*1 configuration (Fig. 3B) than to the more flexible polymer chain in *fm*2 (Fig. 3A). Indeed, at *fm*2, the couple *RR*-chain and *RR*-LA monomer finds a better accommodation rather than at *fm*1, where the monomer points toward the hindered area of the NE quadrant. On the other side, at *fm*2, the monomer lies in the free SW quadrant and the chain avoids clashing, positioning itself on the *z*-axis out of the plane. In the previous considerations, the chirality of the chain also plays an important role in the orientation assumed during the TSs. Indeed, in its conformational minimum, the *RR*-chain at the $C_2$–$O_2$–$C_3$–$C_4$ dihedral angle is $G^+$ (≈+60°), whereas the *SS*-chain at the same dihedral angle is $G^-$ (≈−60°).

The interconversion among *fac–mer* and *fac–fac* is also possible but it requires the energetic evaluation of an

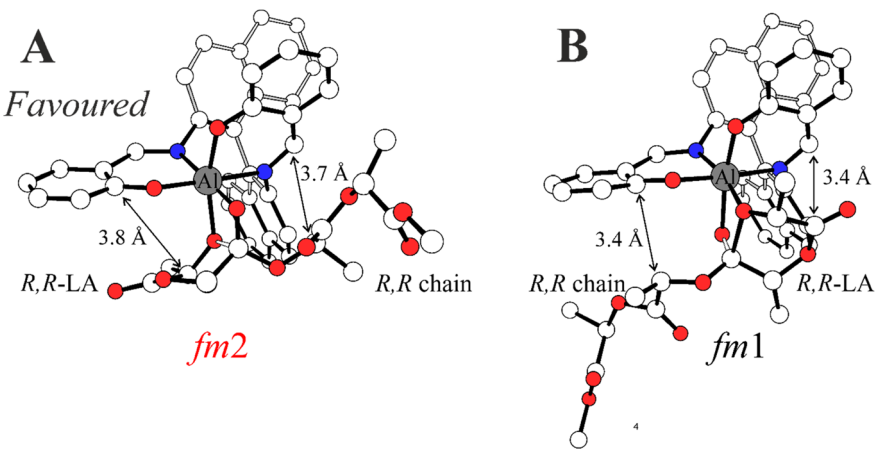


**Fig. 2** Optimized DFT geometries for the RLS of *RR* propagation promoted by (*R*)-**1** corresponding to the ring opening step (TS2). The energetic preference of the *fm*2 wrapping mode (A) with respect to *fm*1 (B) is due to lower steric interactions reported with arrows. Oxygen and nitrogen atoms in red and blue. Distances in Å and H atoms omitted for clarity.

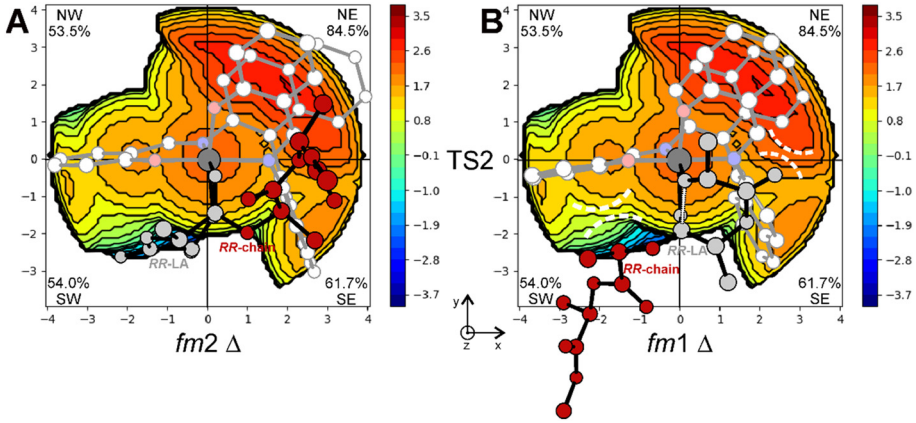


Fig. 3 Steric maps obtained by the % $V_{Bur}$ analysis explaining the energetic preference for *fm*2 (A) *vs.* *fm*1 (B) wrapping modes in the ring opening step (TS2) of *RR*-LA polymerization promoted by the (*R*)-**1** system. The main steric interactions are reported with dashed lines.

additional TS that involves active site reorganization *via* the modification of the $O_L$–Al–$O_L$ valence angle (defined as $\alpha$) from ≈90 to ≈180° (Fig. 4). In Fig. 4A, we report the preferred Gibbs energy path for the mechanism moving from TS1 (in the preferred *fm*1) to TS2 (*ff*) as a function of $\alpha$ for (*RR*)-LA polymerization promoted by (*R*)-**1** and we located the TS for such ligand interconversion at $\alpha$ = 141°, with a barrier of 14.6 kcal $mol^{-1}$ very close to the RLS found for **M2-A** (14.4 kcal $mol^{-1}$, see Fig. 1). These computations suggest that *fm*–*ff* transformation has to be considered in the stereoselectivity computation, increasing the number of mechanistic paths to be computed. However, we noted that such a feature is strictly related to the catalyst flexibility. In our computational screening looking for a simple method to evaluate the ligand wrapping mode energetics, we found that the use of a bidentate ligand such as acetylacetonate ($acac^-$) to simulate the monomer and the growing chain binding appears promising. In fact, the computations with $acac^-$ (Fig. 4B) to mimic the polylactide growing chain avoided the complications derived from the several degrees of freedom of the chain (Fig. 4A), still showing similar energetic profile and geometrical features of TS$\alpha$.

These findings achieved for (*R*)-**1** need to be better discussed and inserted in a more general framework for a comparison with system (*R*,*R*)-**2**. Four different diastereoisomers are derived from the various wrapping modes of the salen ligand around the Al metal center (Scheme 4). These geometries arise from the combination of *fac* and *mer* with Λ and Δ isomerism in the octahedral geometries adopted by the ligand in the ROP TSs (Scheme 3). The *mer*–*mer* isomer was ruled out since the chain and the monomer would be in *trans* of each other, forming an angle of ≈180° (not feasible with the ROP mechanism). Complexes with *ff* or *fm* configurations are inherently chiral and the chirality of the bridge (indicated as X in Scheme 4) "forces" the catalyst to adopt a specific octahedral wrapping mode.

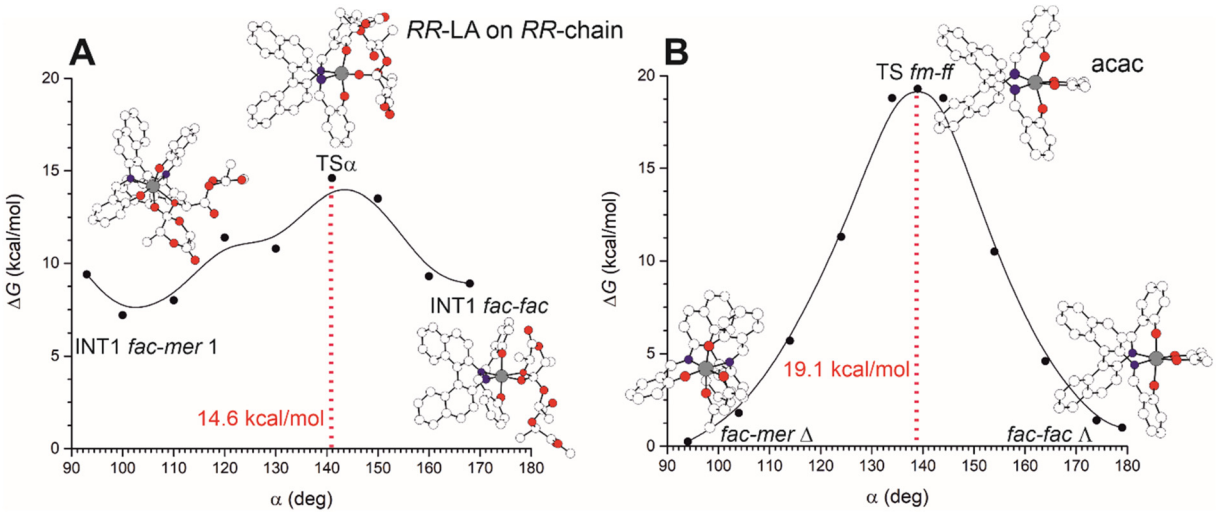


Fig. 4 Free energy profiles of the transformation from *fac*–*mer* Δ to *fac*–*fac* Λ for (*R*)-**1** as a function of the $O_L$–Al–$O_L$ valence bond. The reorganization path moving from TS1 (*fm*1) to TS2 (*ff*) as a function of $\alpha$ for *RR*-LA polymerization is reported in A. The analogous path by using the bidentate $acac^-$ is reported in B. Aluminum, oxygen and nitrogen atoms in gray, red and blue. Hydrogen atoms have been omitted for clarity.

 

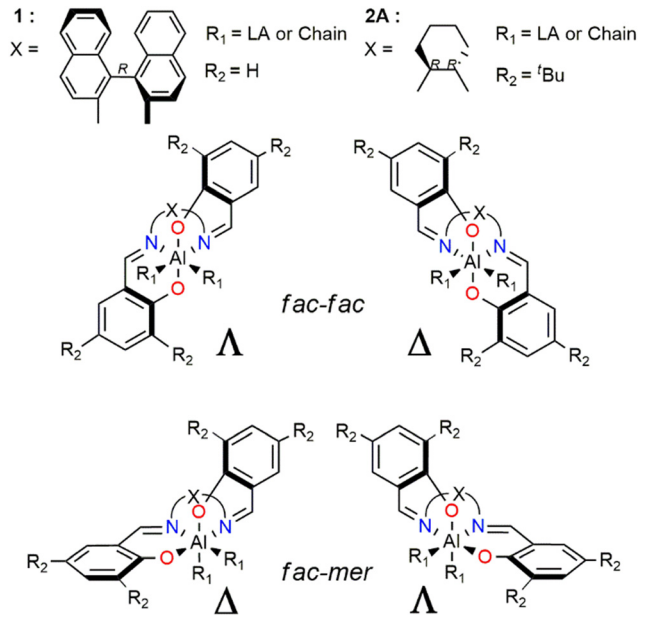


**Scheme 4** Illustrations of the combination of *fac* and *mer* with Λ and Δ isomerism for octahedral chiral salen-type catalysts.

It is worth to note that (*R*)-**1**, bearing X = (*R*)-binaphthyl as the bridge, presents two stable diastereoisomers, *fm* Δ and *ff* Λ which differ only by 1 kcal mol$^{-1}$ (Table 1) due to the flexible binaphthyl linker, constituted by four carbon atoms.

This explains why the *SS*-LA monomer dictates the *ff* configuration of the catalyst (Fig. 1) with a Λ octahedral chirality that is preferred to the *fm* with a Δ octahedral chirality. Indeed, the *SS*-LA polymerization is more easily accommodated in the *ff* Λ wrapping mode (Fig. 5A) than in the *fm* Δ wrapping mode (Fig. 5B) with an energetic preference of 4.0 kcal mol$^{-1}$ (Table S1†). In Fig. 5A, where the favored situation is depicted, the monomer is located in the southern region of the map and the chain lies parallel to the *z*-axis. Steric interactions between the ligand and one of the methyl groups of *SS*-LA are present, explaining the energetic difference in TS1 with *RR*-LA (16.2 *vs.* 12.7 kcal mol$^{-1}$, Fig. 1). However, the situation is additionally disadvantaged with *fm*1 (Fig. 5B), by the fact that the chain is directed toward the hindered SE zone of the map.

It is worth to remark that the *ff* wrapping mode is precluded for (*R*,*R*)-**2A** having X = (*R*,*R*)-cyclohexyl bridge, which is far less flexible being constituted by two carbon atoms. Indeed, in this case, only the *fac–mer* Δ isomer is energetically feasible (Table 1). This important aspect that we will take into account in the following sections sheds a new light on the understanding of chiral catalyst recognition toward *rac*-LA.

**Table 1** Gibbs energy differences (kcal mol$^{-1}$) among the four possible octahedral structures derived from the combination of *fac* and *mer* with Λ and Δ isomerism illustrated in Scheme 4 for (*R*)-**1** and (*R*,*R*)-**2A**. The two $R_1$ moieties were substituted with the symmetric acac$^-$ bidentate ligand

| | Catalyst | |
|---|---|---|
| Diastereoisomers | (*R*)-**1** | (*R*,*R*)-**2A** |
| *fac–mer* Δ | 0.0 | 0.0 |
| *fac–mer* Λ | 29.2 | 8.5 |
| *fac–fac* Δ | 40.2 | 35.9 |
| *fac–fac* Λ | 1.0 | 13.7 |

### 3.2 Stereoselective *rac*-LA ROP promoted by (*R*,*R*)-2A and (*R*,*R*)-2B

System (*R*,*R*)-**2A** experimentally shows a clear preference toward the *SS*-LA monomer in the ROP of *rac*-LA (Scheme 2), although the *ff* wrapping mode that leads the *SS*-LA propagation for (*R*)-**1** is too high in energy (Table 1 and ESI†). This implies that the AKRP origin of (*R*,*R*)-**2A** should be traced within the *fm* Δ wrapping mode. The simplified MEP of *rac*-LA isotactic enchainment extracted from a combinatorial analysis of all the elements of chirality (Tables S2 and S3†) is summarized in Fig. 6. The energetic preference for *SS*-LA (Fig. 6-left) *vs.* *RR*-LA (Fig. 6-right) propagation is sorted out by our DFT results, and the calculated stereoselectivity (ΔΔ*G* of 2.2 kcal mol$^{-1}$, Fig. 6) matches with the experimental results (Scheme 2). However, the preferred *SS*-LA energetic enchainment shows a *fm*2 wrapping mode (**M1-B** mechanism) and the RLS for this enchainment (TS1, 11.3 kcal mol$^{-1}$) is preferred to the analogous having fm1 configuration (18.8 kcal mol$^{-1}$, Fig. S1 and Table S2†). The preference for *fm*2 is also maintained for the low-lying *RR*-LA enchainment (Table S3†), although the free energies are upshifted (13.5 kcal mol$^{-1}$), consistent with the experimental preference. The calculated enantioselectivity (ΔΔ*G* among the two RLSs at *fm*2) is similar to that of catalyst (*R*)-**1**, (≈2 kcal mol$^{-1}$) and analogously, we found the switching of *fm* configurations going from TS1 to TS2 for *RR*-LA propagation (comparing the **M2-B** mechanism in Fig. 6 with **M2-A** in Fig. 3). Such a mechanism helps in a better refinement of the MEP, the TS2 at *fm*2 being 2.4 kcal mol$^{-1}$ higher than the TS2 at *fm*1 so a much higher enantioselectivity (3.6 kcal mol$^{-1}$) would have been predicted.

Once a reasonable agreement with the experimental data is achieved, the origin of the stereoselectivity can be rationalized. In particular, the high steric hindrance exerted by bulky $^t$Bu groups in the *ortho* position of the (*R*,*R*)-**2A** system is crucial for inferring a stereoselective outcome to this reaction. This feature can be visualized by the % $V_{Bur}$ steric maps reported in Fig. 7. Indeed, TS1 for *SS* propagation accommodates both the monomer and the growing chain in the least hindered area of the ligand (Fig. 7A). For *RR* propagation, the orientation of the *RR*-chain points towards the SW occupied by $^t$Bu groups (Fig. 7B), justifying the energetic difference between the two RLSs determining the enantioselectivity. As a matter of fact, the conformation of the chain with the steric hindrance exerted by the ligand pushes the disfavored axial positioning of the lactide methyl substituents of the nucleophilic addition TS (Fig. S2†). Lastly, the % $V_{Bur}$ steric maps also explain the energetic reason for

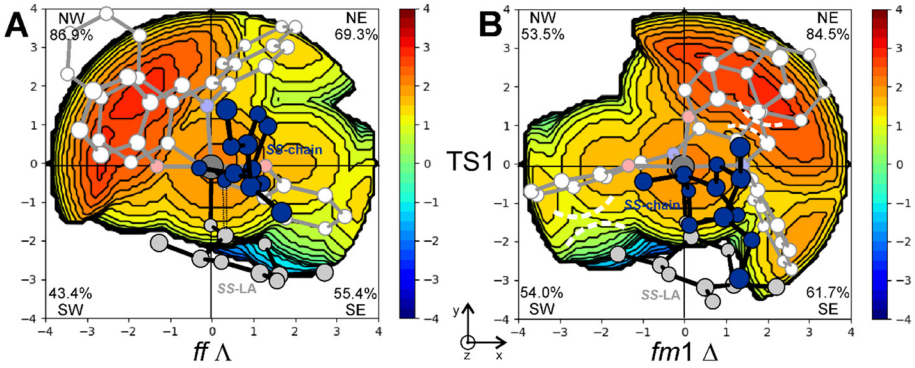


Fig. 5 Steric maps obtained by the % $V_{Bur}$ analysis explaining the wrapping mode energetic preference for *ff* (A) *vs. fm*1 (B) configurations in the nucleophilic addition step (TS1) of *SS*-LA polymerization promoted by the (*R*)-**1** system. Main steric interactions are reported with dashed lines.

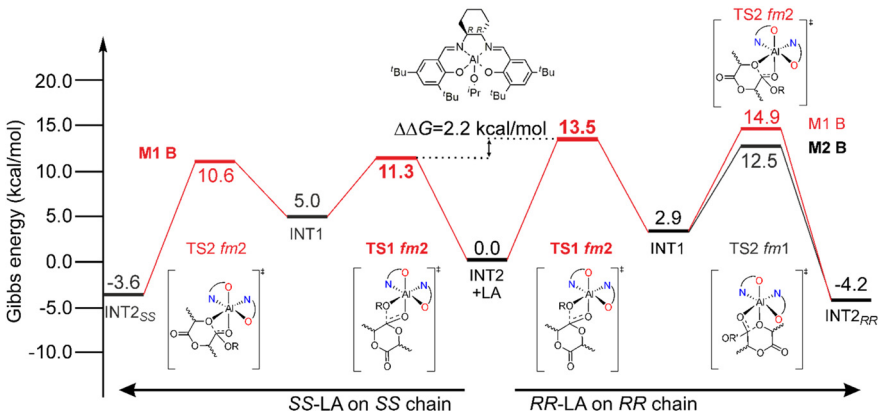


Fig. 6 Preferred Gibbs energy paths for *SS*-LA (left) and *RR*-LA (right) propagations promoted by the (*R,R*)-**2A** system following the **M1**–**M2** mechanisms. The RLSs for the reaction paths (see text) are reported in bold.

the switching of the monomer and growing chain positions in the ring opening step (TS2) with *fm*1 (Fig. 7C) having less unfavorable interactions with respect to *fm*2 conformations (Fig. 7D).

The importance of $^t$Bu groups in the *ortho* position has been further confirmed by computing the stereoselectivity of the (*R,R*)-**2B** system (replacing $^t$Bu with H atoms) in the *rac*-LA polymerization. The calculated enantioselectivity of (*R,R*)-**2B** decreases to 0.5 kcal mol$^{-1}$ (RLS structures are reported in Fig. S3†), in good agreement with recent experimental data by Wang *et al.* who claimed a poor stereoselectivity in the ROP of *rac*-LA toward *SS*-LA promoted by (*R,R*)-**2B**.[25] The % $V_{Bur}$ steric maps of the RLS for *SS*-LA (Fig. 8A) and *RR*-LA (Fig. 8B) obtained with (*R,R*)-**2B** show that the occupancies of NW and SW quadrants drop respectively to 57.1% and 43.9% from 76.5% and 49.2% calculated for (*R,R*)-**2A** (Fig. 7A and B).

The DFT energetic plots in Fig. 1 and 6, combined with steric maps in Fig. 3 and 5, rationalized the origin of ESC control in the *rac*-LA ROP promoted by (*R*)-**1** (*RR* preference) and by (*R,R*)-**2A** (*SS* preference) including the intermediate situation of (*R,R*)-**2B**. The multiple mechanistic paths we proposed are the only way to explain the experimental data (Table S4†). However, additional insights are disclosed by computing the activation Gibbs energies for all enchainments, including the *RR* and *SS* insertions on *SS*- and *RR*-chains, respectively. The main results summarized in Table 2 (complete lists reported in Tables S5 and S6†) suggest that the occasional insertion of *SS*-LA is corrected by the ESC of (*R*)-**1** being the heterotactic enchainment intermediate between the isotactic ones (Table 2-left and Fig. S4†). Occasional *RR* insertion at (*R,R*)-**2A** are, instead, favoured by the last inserted *RR*-chain (Table 2-right and Fig. S5†). The additional CEC interplay we found might explain the isotactic stereosequences reported by Nomura *et al.*[29] in the *rac*-LA ROP promoted by an achiral salen catalyst (X = Et; $R_2$ = $^t$Bu, Scheme 4) as well as the subtle microstructure differences of PLA stereoblocks obtained by (*R*)-**1** and (*R,R*)-**2A**.

## 4. Conclusions

This computational study revealed the origin of the stereoselectivity in the *rac*-LA ROP promoted by two enantiopure salen–Al systems which have so far been claimed as the most stereoselective catalysts through ESC control.[5,6] Despite belonging to the same ligand class, (*R*)-**1** and (*R,R*)-**2A** preferentially select opposite enantiomers in the polymerization of *rac*-LA. We succeeded in explaining the experimental stereoselectivity, and our

 

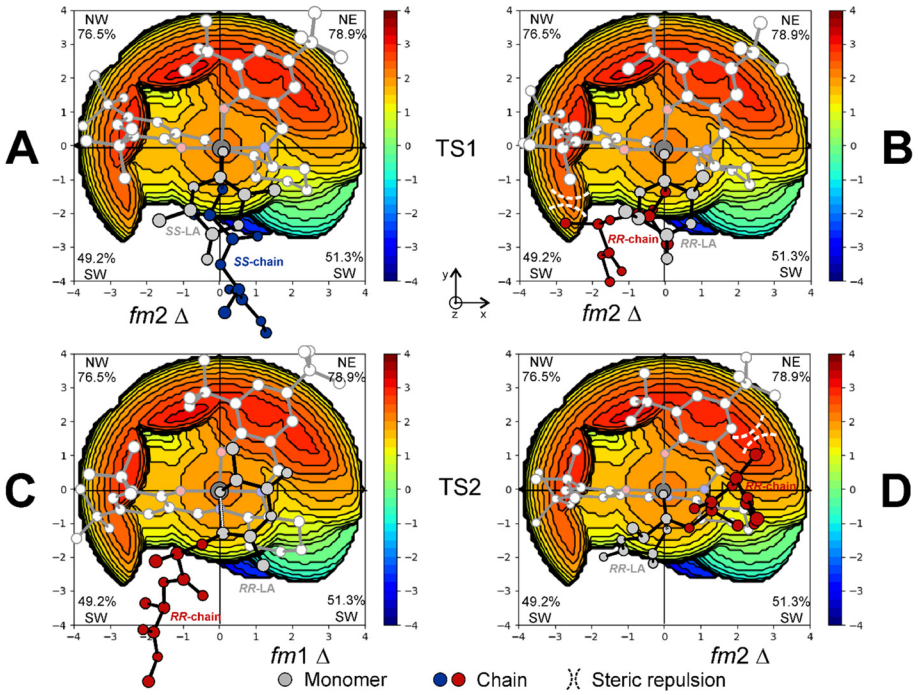


**Fig. 7** % $V_{Bur}$ steric maps of the RLS corresponding to TS1 for *SS*-LA (A) and *RR*-LA (B) propagations with catalyst (*R*,*R*)-**2A**. Steric interactions leading to the TS2 preference for *fm*1 (C) *vs. fm*2 (D) for *RR*-LA propagation are reported with dashed lines. The *z*-axis is perpendicular to the plane containing the map.

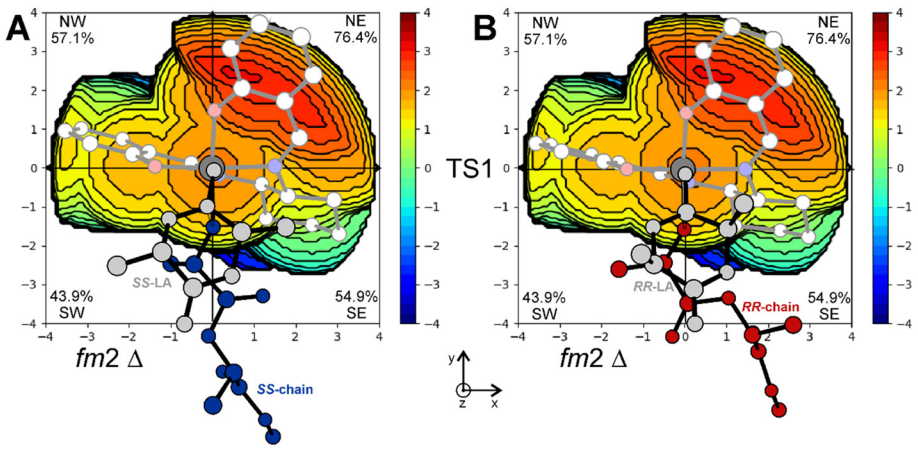


**Fig. 8** % $V_{Bur}$ steric maps of the RLS corresponding to TS1 for *SS*-LA (A) and *RR*-LA (B) propagation with catalyst (*R*,*R*)-**2B**.

**Table 2** Activation Gibbs energies for the RLS ($\Delta G^{\ddagger}_{RLS}$) and activation Gibbs energy differences ($\Delta\Delta G$ relative to the most stable path) for *RR*-LA and *SS*-LA propagations promoted by (*R*)-**1** (left) and (*R*,*R*)-**2A** (right) depending on the assembly mode

| System (*R*)-**1** | | | System (*R*,*R*)-**2A** | | |
|---|---|---|---|---|---|
| Assembly mode | $\Delta G^{\ddagger}_{RLS}$ (kcal mol$^{-1}$) | $\Delta\Delta G$ (kcal mol$^{-1}$) | Assembly mode | $\Delta G^{\ddagger}_{RLS}$ (kcal mol$^{-1}$) | $\Delta\Delta G$ (kcal mol$^{-1}$) |
| *RR*-LA + *RR* chain | 14.4 | 0.0 | *SS*-LA + *SS* chain | 11.3 | 0.0 |
| *RR*-LA + *SS* chain | 14.9 | 0.5 | *RR*-LA + *RR* chain | 13.5 | 2.2 |
| *SS*-LA + *RR* chain | 15.2 | 0.8 | *RR*-LA + *SS* chain | 13.9 | 2.6 |
| *SS*-LA + *SS* chain | 16.2 | 1.8 | *SS*-LA + *RR* chain | 14.5 | 3.2 |

analysis provided additional insights. First, the presence of a chiral flexible bridge, such as (*R*)-binaphthyl in (*R*)-**1**, makes both *ff* and *fm* octahedral wrapping modes feasible, with their energetic preference dictated by the monomer's chirality. This feature, combined with multiple possible reaction pathways due to the easy switching of the

monomer and chain positions, explains (*R*)-**1**'s preference for forming PDLA from *rac*-LA.

In contrast, with a less flexible chiral bridge, such as (*R*,*R*)-cyclohexyl in (*R*,*R*)-**2A**, access to *ff* chiral octahedral wrapping modes is precluded. However, multiple monomer-controlled reaction paths remain. The stereoselective outcome, in this case, is ensured by a fixed chiral octahedral environment enforced by the steric hindrance of the $^{t}$Bu groups in the *ortho* position of the salen ligand, leading to the preferred formation of PLLA from *rac*-LA. This feature was further confirmed by modeling the ROP of *rac*-LA promoted by (*R*,*R*)-**2B**, which has H atoms in the *ortho* position, resulting in a lower AKRP.[25]

Finally, the DFT calculations of the overall microstructures revealed the interplay between ESC and CEC, opening the way to rationalize the CEC promoted by achiral salen systems.[29] We believe that the insights from this work can be useful for both the theoretical and experimental communities in the rational development of ROP stereoselective catalysts,[45] thereby bridging the gap with TM-catalyzed olefin polymerization.[46]

## Data availability

Data for this article including computational details, Scheme S1, Fig. S1–S5, Tables S1–S6,† and Cartesian coordinates (*xyz*) of the MEP structures mentioned in the text are available free of charge at **https://doi.org/10.1039/d4cy00937a**.

## Conflicts of interest

There are no conflicts to declare.

## Acknowledgements

This work was financially supported by the Italian Ministry of University and Research (PRIN 2022, CUP E53D23008360006). This study was carried out within the MICS (Made in Italy-Circular and Sustainable) Extended Partnership funded from the European Union Next-Generation EU (Piano Nazionale di Ripresa e Resilienza (PNRR)–Missione 4 Componente 2, Investimento 1.3 – D.D. 1551.11-10-2022, PE00000004).

## References

1 F. Vidal, E. R. van der Marel, R. W. F. Kerr, C. McElroy, N. Schroeder, C. Mitchell, G. Rosetto, T. T. D. Chen, R. M. Bailey, C. Hepburn, C. Redgwell and C. K. Williams, *Nature*, 2024, **626**, 45–57.
2 C. Shi, E. C. Quinn, W. T. Diment and E. Y. X. Chen, *Chem. Rev.*, 2024, **124**, 4393–4478.
3 S. Lambert and M. Wagner, *Chem. Soc. Rev.*, 2017, **46**, 6855–6871.
4 E. Castro-Aguirre, F. Iñiguez-Franco, H. Samsudin, X. Fang and R. Auras, *Adv. Drug Delivery Rev.*, 2016, **107**, 333–366.
5 C. M. Thomas, *Chem. Soc. Rev.*, 2010, **39**, 165–173.
6 M. J. Stanford and A. P. Dove, *Chem. Soc. Rev.*, 2010, **39**, 486–494.
7 L. Resconi, L. Cavallo, A. Fait and F. Piemontesi, *Chem. Rev.*, 2000, **100**, 1253–1346.
8 V. Busico, R. Cipullo, R. Pellecchia, S. Ronca, G. Roviello and G. Talarico, *Proc. Natl. Acad. Sci.*, 2006, **103**, 15321–15326.
9 N. Bahri-Laleh, A. Hanifpour, S. A. Mirmohammadi, A. Poater, M. Nekoomanesh-Haghighi, G. Talarico and L. Cavallo, *Prog. Polym. Sci.*, 2018, **84**, 89–114.
10 L. Cavallo, *Polymer*, 2024, **291**, 126589.
11 M. J. L. Tschan, R. M. Gauvin and C. M. Thomas, *Chem. Soc. Rev.*, 2021, **50**, 13587–13608.
12 H. Tsuji, *Adv. Drug Delivery Rev.*, 2016, **107**, 97–135.
13 X. Li, Z. Jia, X. Pan and J. Wu, *Chem. – Asian J.*, 2019, **14**, 662–669.
14 N. Yuntawattana, T. M. McGuire, C. B. Durr, A. Buchard and C. K. Williams, *Catal. Sci. Technol.*, 2020, **10**, 7226–7239.
15 X. Pang, R. Duan, X. Li, C. Hu, X. Wang and X. Chen, *Macromolecules*, 2018, **51**, 906–913.
16 P. Daneshmand, A. van der Est and F. Schaper, *ACS Catal.*, 2017, **7**, 6289–6301.
17 R. Hador, A. Botta, V. Venditto, S. Lipstman, I. Goldberg and M. Kol, *Angew. Chem., Int. Ed.*, 2019, **58**, 14679–14685.
18 W. Rao, C. Cai, J. Tang, Y. Wei, C. Gao, L. Yu and J. Ding, *Chin. J. Chem.*, 2021, **39**, 1965–1974.
19 W.-H. Rao, L. Yu and J.-D. Ding, *Chin. J. Polym. Sci.*, 2023, **41**, 745–759.
20 X. Wang, Y. Huang, X. Xie, Y. Liu, Z. Huo, M. Lin, H. Xin and R. Tong, *Nat. Commun.*, 2023, **14**, 3647.
21 C. De Rosa, R. Di Girolamo, A. B. Muñoz-García, M. Pavone and G. Talarico, *Macromolecules*, 2020, **53**, 2959–2964.
22 N. Spassky, M. Wisniewski, C. Pluta and A. Le Borgne, *Macromol. Chem. Phys.*, 1996, **197**, 2627–2637.
23 T. M. Ovitt and G. W. Coates, *J. Am. Chem. Soc.*, 2002, **124**, 1316–1326.
24 Z. Zhong, P. J. Dijkstra and J. Feijen, *J. Am. Chem. Soc.*, 2003, **125**, 11291–11298.
25 Z. Peng, H. Ahmed, G. Xu, X. Guo, R. Yang, H. Sun and Q. Wang, *Polym. Chem.*, 2023, **14**, 2174–2180.
26 P. McKeown, M. G. Davidson, G. Kociok-Köhn and M. D. Jones, *Chem. Commun.*, 2016, **52**, 10431–10434.
27 S. M. Kirk, G. Kociok-Köhn and M. D. Jones, *Organometallics*, 2016, **35**, 3837–3843.
28 K. Press, I. Goldberg and M. Kol, *Angew. Chem., Int. Ed.*, 2015, **54**, 14858–14861.
29 N. Nomura, R. Ishii, Y. Yamamoto and T. Kondo, *Chem. – Eur. J.*, 2007, **13**, 4433–4451.
30 P. Hormnirun, E. L. Marshall, V. C. Gibson, R. I. Pugh and A. J. P. White, *Proc. Natl. Acad. Sci. U. S. A.*, 2006, **103**, 15343–15348.
31 S. M. Guillaume, E. Kirillov, Y. Sarazin and J.-F. Carpentier, *Chem. – Eur. J.*, 2015, **21**, 7988–8003.
32 M. H. Chisholm, J. C. Gallucci, K. T. Quisenberry and Z. Zhou, *Inorg. Chem.*, 2008, **47**, 2613–2624.
33 M. C. D'Alterio, C. De Rosa and G. Talarico, *ACS Catal.*, 2020, **10**, 2221–2225.

 

34 M. C. D'Alterio, C. De Rosa and G. Talarico, *Chem. Commun.*, 2021, **57**, 1611–1614.
35 X. Guo, G. Xu, R. Yang and Q. Wang, *J. Am. Chem. Soc.*, 2024, **146**, 9084–9095.
36 A. Grillo, Y. Rusconi, M. C. D'Alterio, C. De Rosa, G. Talarico and A. Poater, *Int. J. Mol. Sci.*, 2024, **25**, 1647.
37 Y. Rusconi, M. C. D'Alterio, A. Grillo, A. Poater, C. De Rosa and G. Talarico, *Polymer*, 2024, **292**, 126639.
38 Y. Rusconi, M. C. D'Alterio, C. De Rosa, Y. Lu, S. M. Severson, G. W. Coates and G. Talarico, *ACS Catal.*, 2024, **14**, 318–323.
39 E. Romano, V. Barone, P. H. M. Budzelaar, C. De Rosa and G. Talarico, *Chem. – Asian J.*, 2024, **19**, e202400155.
40 O. D'Anania, E. Romano, V. Barone and G. Talarico, *J. Comput. Chem.*, 2024, **45**, 1483–1492.
41 L. Falivene, V. Barone and G. Talarico, *Mol. Catal.*, 2018, **452**, 138–144.
42 L. Falivene, Z. Cao, A. Petta, L. Serra, A. Poater, R. Oliva, V. Scarano and L. Cavallo, *Nat. Chem.*, 2019, **11**, 872–879.
43 S. Escayola, N. Bahri-Laleh and A. Poater, *Chem. Soc. Rev.*, 2024, **53**, 853–882.
44 L. Falivene, L. Cavallo and G. Talarico, *ACS Catal.*, 2015, **5**, 6815–6822.
45 X. Tang, A. H. Westlie, L. Caporaso, L. Cavallo, L. Falivene and E. Y.-X. Chen, *Angew. Chem., Int. Ed.*, 2020, **59**, 7881–7890.
46 J. W. Han, F. Hollmann, R. Luque, I. K. Song, G. Talarico, T. Tatsumi and N. Yan, *Mol. Catal.*, 2022, **522**, 112233.